

# Thermoelectric Characterization Platform for Electrochemically Deposited Materials

Vida Barati, Javier Garcia Fernandez, Kevin Geishendorf, Lauritz Ule Schnatmann, Michaela Lammel, Alexander Kunzmann, Nicolás Pérez, Guodong Li, Gabi Schierning, Kornelius Nielsch, and Heiko Reith\*

Successful optimization of the thermoelectric (TE) performance of materials, described by the figure of merit  $zT$ , is a key enabler for its application in energy harvesting or Peltier cooling devices. While the  $zT$  value of bulk materials is accessible by a variety of commercial measurement setups, precise determination of the  $zT$  value for thin and thick films remains a great challenge. This is particularly relevant for films synthesized by electrochemical deposition, where the TE material is deposited onto an electrically conductive seed layer causing an in-plane short circuit. Therefore, a platform for full in-plane  $zT$  characterization of electrochemically deposited TE materials is developed, eliminating the impact of the electrically conducting seed layer. The characterization is done using a suspended TE material within a transport device which was prepared by photolithography in combination with chemical etching steps. An analytical model to determine the thermal conductivity is developed and the results verified using finite element simulations. Taken together, the full in-plane  $zT$  characterization provides an inevitable milestone for material optimization under realistic conditions in TE devices.

Things devices,<sup>[9]</sup> and body-powered wearable electronics.<sup>[10,11]</sup> Consequently, there is a demand for the characterization of TE materials with small geometrical dimension, like nano- and micro-scaled thin or thick films.<sup>[12–14]</sup> Compared with nano-scaled TE films, micro-scaled TE films are more desirable for  $\mu$ TEDs due to the low electrical resistance and high attainable densities of heat flux and cooling power.<sup>[8]</sup> The increasing interest in micro-scaled TE materials motivated the development of different characterization techniques dedicated to determine the figure of merit  $zT$ , defined by the Seebeck coefficient  $\alpha$ , electrical conductivity  $\sigma$ , thermal conductivity  $\lambda$ , and absolute temperature  $T$ .

$$zT = \frac{\alpha^2 \sigma}{\lambda} T \quad (1)$$


## 1. Introduction

Thermoelectricity describes a direct transformation between heat fluxes and electricity or vice versa. TE devices can be operated either as TE generator or as Peltier cooler.<sup>[1–3]</sup> Among them, micro-TE devices ( $\mu$ TEDs) received considerable attraction because of many prospective applications such as thermal management,<sup>[4–6]</sup> cooling of power electronics,<sup>[7,8]</sup> the Internet of

Things devices,<sup>[9]</sup> and body-powered wearable electronics.<sup>[10,11]</sup> Consequently, there is a demand for the characterization of TE materials with small geometrical dimension, like nano- and micro-scaled thin or thick films.<sup>[12–14]</sup> Compared with nano-scaled TE films, micro-scaled TE films are more desirable for  $\mu$ TEDs due to the low electrical resistance and high attainable densities of heat flux and cooling power.<sup>[8]</sup> The increasing interest in micro-scaled TE materials motivated the development of different characterization techniques dedicated to determine the figure of merit  $zT$ , defined by the Seebeck coefficient  $\alpha$ , electrical conductivity  $\sigma$ , thermal conductivity  $\lambda$ , and absolute temperature  $T$ .

One of the challenges when seeking for highly efficient TE materials with nano- and micro scaled geometry is the difficulty to exactly assess their  $zT$  values. This is in particular valid for thick films grown by the electrochemical deposition technique, which is often used in the fabrication of  $\mu$ TEDs. In this latter case, TE materials are deposited onto an electrically conductive seed layer which causes a short circuit to the in-plane electrical field. This makes the unambiguous determination of the transport coefficients hard to achieve.

V. Barati, Dr. J. Garcia Fernandez, K. Geishendorf, L. U. Schnatmann, M. Lammel, A. Kunzmann, Dr. N. Pérez, Dr. G. Li, Dr. G. Schierning, Prof. K. Nielsch, Dr. H. Reith  
 Institute for Metallic Materials  
 Leibniz Institute for Solid State and Materials Research Dresden  
 Helmholtzstraße 20 01069, Dresden, Germany  
 E-mail: h.reith@ifw-dresden.de

 The ORCID identification number(s) for the author(s) of this article can be found under <https://doi.org/10.1002/aelm.201901288>.

© 2020 The Authors. Published by WILEY-VCH Verlag GmbH & Co. KGaA, Weinheim. This is an open access article under the terms of the Creative Commons Attribution-NonCommercial License, which permits use, distribution and reproduction in any medium, provided the original work is properly cited and is not used for commercial purposes.

DOI: 10.1002/aelm.201901288

V. Barati, Prof. K. Nielsch  
 Institute of Materials Science  
 Dresden University of Technology  
 01062, Dresden, Germany

Dr. J. Garcia Fernandez  
 Department of Physics  
 University of Oviedo  
 C/Federico Garcia Lorca no 18 33007, Oviedo, Spain

K. Geishendorf, L. U. Schnatmann, M. Lammel, Prof. K. Nielsch  
 Institute of Applied Physics  
 Dresden University of Technology  
 01062, Dresden, Germany

Dr. G. Li  
 Beijing National Laboratory for Condensed Matter Physics  
 Institute of Physics  
 Chinese Academy of Sciences  
 Beijing 100190, China

There are different methods to determine the  $zT$  value of nano- and micro-scaled films experimentally. One common approach is to measure the single transport coefficients in separate setups, often done using different samples.<sup>[15,16]</sup> Only few approaches are able to characterize the  $zT$  value simultaneously on the same sample.<sup>[13,17,18]</sup> For instance, the Harman method has been used to characterize cross-plane  $zT$  values of thin film superlattice structures.<sup>[14,19,20]</sup> Another full in-plane  $zT$  characterization of nano-scaled TE films based on a pre-structured measurement device was presented by Linseis et al.<sup>[18,21]</sup> Nevertheless, since the film has to be deposited on the pre-structured measurement device, combining structures for van der Pauw and Joule heating methods, it is not possible to remove the seed layer required for electrochemical deposition. Therefore, the device cannot be used for the characterization of electrochemically deposited films.

In this study, we demonstrate a transport device for the complete steady state characterization of TE thick films grown by electrochemical deposition. Our transport device enables the simultaneous characterization of the in-plane  $\alpha$ ,  $\sigma$ , and  $\lambda$  of the TE thick film, avoiding the falsification of the data by the influence of the substrate and the conductive seed layer. We successfully designed a transport device to characterize the electrochemically deposited cobalt nickel alloy with the composition of 75 % of Co and 25 % of Ni. This composition has a high TE power factor ( $PF > 4 \text{ mW m}^{-1} \text{ K}^{-2}$ ) as well as an excellent reproducibility of the electrochemical deposition, well-established by a variety of different available deposition parameters, also in the pre-structured transport device.<sup>[22–24]</sup>

## 2. Results and Discussion

### 2.1. Conceptual Approach

The characterization was performed using a transport device which in its turn acts as a substrate for the electrochemically deposited TE material. In **Figure 1**, a top view of the transport device layout with a detailed view of its center region is shown. A  $\text{Si}_3\text{N}_4$  membrane was structured in the center of the device on which an electrically conductive seed layer, the heating stripe, four electrodes, and the TE material were patterned. The heating stripe was placed in the center of the structure, partly passivated by a  $\text{SiO}_2$  layer. Four electrodes placed symmetrically on both sides of the heating stripe served as resistance

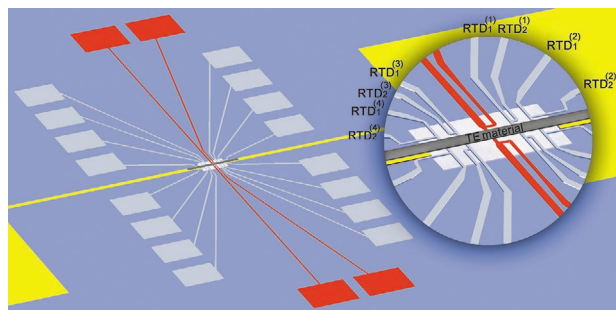


**Figure 1.** A top view of the transport device with an inset of its center including a heating stripe (red), four electrodes (light gray), the electrically conductive seed layer Au (yellow), and the TE material (dark gray).

temperature detectors (RTDs). To finalize the transport device, the seed layer was removed by wet chemical etching after TE deposition to eliminate its impact on the characterization. This configuration allowed a full in-plane  $zT$  characterization of an electrodeposited TE material.

### 2.2. Fabrication of the Transport Device

The transport device was fabricated by a process comprising photolithographic structuring, sputter deposition, reactive ion etching (RIE), atomic layer deposition (ALD), anisotropic KOH etching of silicon, as well as wet cleaning and etching process of Au and Cr (see **Figure 2a–i** and Supporting Information for details of the process flow). As substrate, a Si wafer (gray) of 300  $\mu\text{m}$  thickness with a 100 nm  $\text{Si}_3\text{N}_4$  layer (blue) on both sides was used. In the first step, a rectangular window of  $520 \times 460 \mu\text{m}^2$  was structured on the backside of the substrate by photolithography and RIE of the  $\text{Si}_3\text{N}_4$  layer (see **Figure 2a,b**). The uncovered Si was anisotropically etched using an aqueous KOH solution, until the front  $\text{Si}_3\text{N}_4$  layer was reached (see **Figure 2c**). The result of this etching was a free standing  $\text{Si}_3\text{N}_4$  membrane of  $100 \times 40 \mu\text{m}^2$  within a defined cavity, that served as a substrate for the deposition of the TE thick film.

In the next step, a conductive seed layer for electrochemical deposition of the TE material was patterned on the front side of the free-standing  $\text{Si}_3\text{N}_4$  membrane by photolithographic structuring and sputtering of 10 nm Cr and 150 nm Au as adhesion and seed layer, respectively (see **Figure 2d**). Hereafter, the heating stripe, four RTDs, and the contact pads were patterned by a 10 nm Ti and a 400 nm Pt as adhesion and contact layer in a lift-off process (see **Figure 2e**). Subsequently, a 50 nm  $\text{SiO}_2$  passivation layer was deposited by ALD. This passivation layer served as electrical insulation between the heating stripe and the TE material. For later electrical contacting and electrochemical deposition, the  $\text{SiO}_2$  layer was removed from the RTDs, the seed layer, and the contact pads using photolithographic patterning in combination with RIE (see **Figure 2f**). Afterward, we electrochemically deposited 6  $\mu\text{m}$   $\text{Co}_{75}\text{Ni}_{25}$  under pulsed potentiostatic conditions in a three-electrode configuration on the pre-structured substrate (**Figure 2g**). A detailed description of the electrochemical deposition is given in Section 4 Electrochemical Deposition.

**Figure 2h,i** shows schematically the finalization of the transport device. First, the  $\text{Si}_3\text{N}_4$  membrane was etched from the backside using RIE followed by wet-chemical etching of the Cr adhesion layer and the Au seed layer to obtain suspended TE material. In **Figure 3**, optical microscope (OM) images of the sample before (a) and after (b) backside etching are shown. More details of the device can be seen in an OM image of its front side (see **Figure 3c**). As a result of the etching process, the free standing heating stripe (red), RTDs (light gray), and TE material (dark gray) deposited on the top side of the membrane were revealed. The front side of the finalized transport device is shown in a scanning electron microscopic (SEM) image (see **Figure 3d**), where the suspended TE material can be well distinguished. Note that color codes are used for easy identification of different materials and functionalities within the device to enable a direct

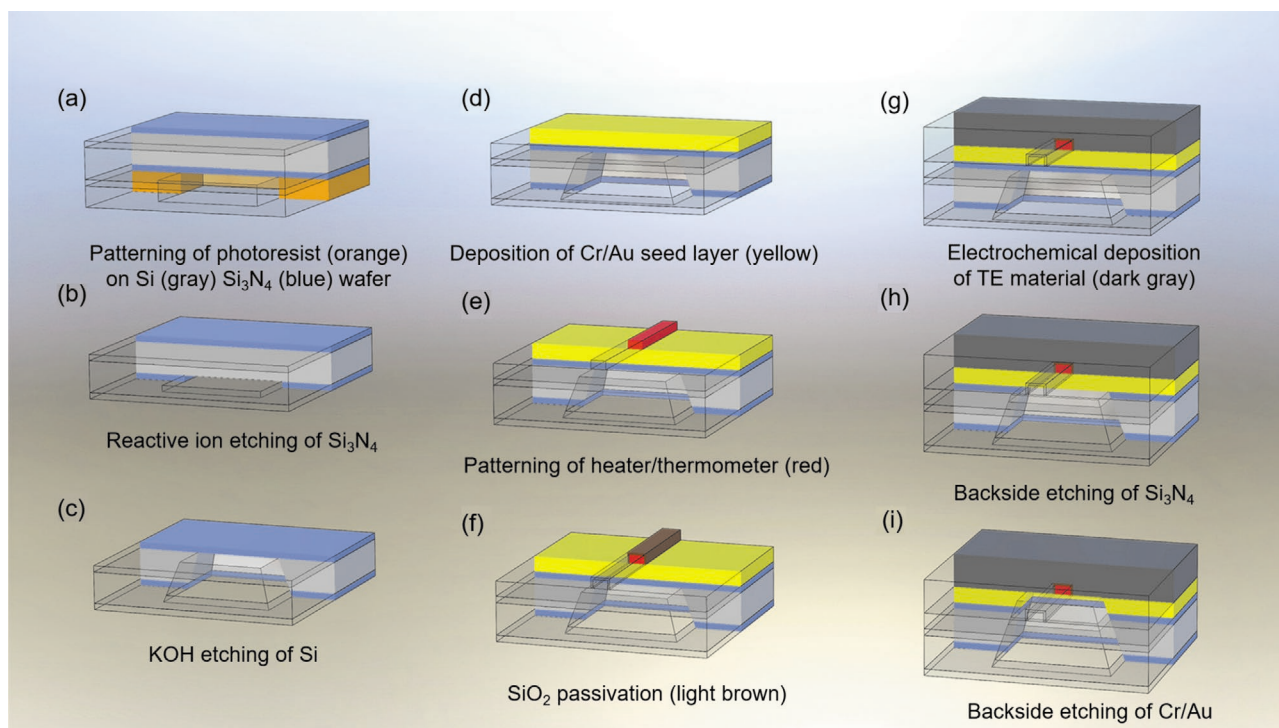


**Figure 2.** Schematic process flow showing the fabrication of the transport device. a) patterning of photoresist (orange) on an  $\text{Si}_3\text{N}_4$  (blue)-coated Si (gray) substrate, b) removal of  $\text{Si}_3\text{N}_4$  by RIE, c) anisotropic etching of Si by KOH etching, d) deposition of Cr/Au adhesion and seed layer (yellow) by sputtering, e) patterning of the heating stripe and the RTDs (red), f) protecting the heating stripe by a dielectric layer  $\text{SiO}_2$  layer (light brown), g) electrochemical deposition of TE material (dark gray), h) backside etching of  $\text{Si}_3\text{N}_4$ , and i) wet chemical etching of Cr/Au adhesion and seed layer.

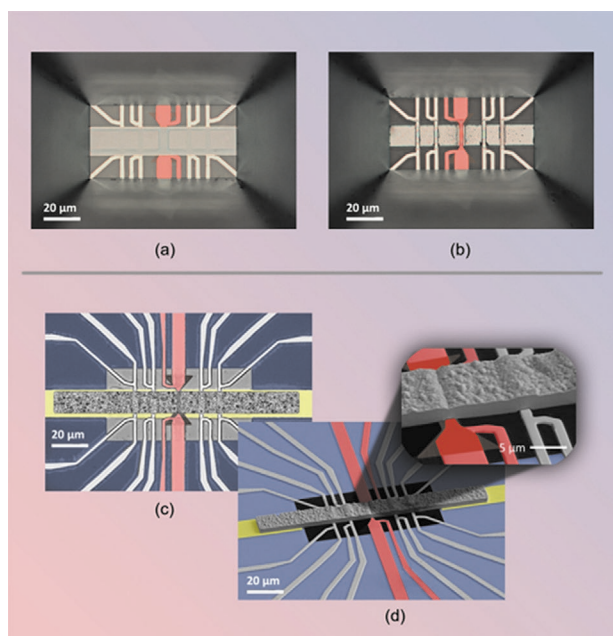


**Figure 3.** a) An OM image of backside of the initial transport device before backside etching, b) an OM image of backside of the transport device after etching the  $\text{Si}_3\text{N}_4$  and the Cr/Au adhesion and seed layer, c) an OM image top view of the transport device before backside etching, and d) a SEM image top view of the transport device after backside etching. The inset in the center shows a nice view of the heating stripe with the  $\text{SiO}_2$  passivation and the TE material.

comparison with the schematic pictures. The dimension of the heating stripe and accordingly its  $\text{SiO}_2$  passivation was chosen in a way that enables the growth of the TE material across the small passivated section building a dell at the intersection area (see inset in Figure 3d).

### 2.3. Electrical Conductivity Characterization Procedure

The electrical conductivity of the sample was determined in a common 4-point probe configuration using contacts from the RTDs on both sides of the heating stripe. **Figure 4a** shows schematically the used contact configuration for the measurement of the electrical conductivity. A current  $I_{4p}$  was applied between the contacts  $\text{RTD}_1^{(4)}$  and  $\text{RTD}_1^{(2)}$  creating a voltage drop  $V_{4p}$  between the voltage probes  $\text{RTD}_1^{(3)}$  and  $\text{RTD}_1^{(1)}$  (see Figure 4a). The electrical conductivity was calculated from  $\sigma = L_{4p} R_{4p}^{-1} A^{-1}$ , with the resistance  $R_{4p} = V_{4p} I_{4p}^{-1}$ , the distance  $L_{4p}$  between the voltage probes, and the cross-section  $A$  of the deposited TE material.

### 2.4. Seebeck Coefficient Characterization Procedure

For the characterization of the Seebeck coefficient, the heating stripe in the center of the membrane and the RTDs were used (see Figure 4b).  $\text{RTD}^{(1)}$  and  $\text{RTD}^{(3)}$  close to the heating stripe were used as hot contacts, while  $\text{RTD}^{(2)}$  and  $\text{RTD}^{(4)}$  located near the edge of the surrounding Si were used as cold contacts. By

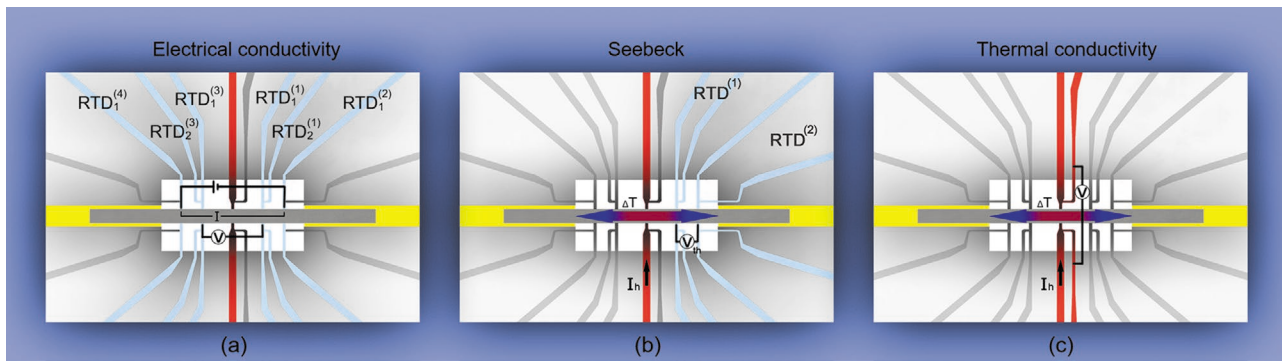


**Figure 4.** a) A schematic view of the  $\sigma$  measurement setup, b) a schematic view of the  $\alpha$  measurement setup, and c) a schematic view of the  $\lambda$  measurement setup.

applying an electrical current to the heating stripe, a temperature gradient was created across the sample from the heating stripe to both edges of the surrounding Si which served as heat sink. The temperature increase  $(T - T_0)$  of each RTD was measured by evaluating its resistance increase  $R(T) - R(T_0)$  with respect to the ambient temperature  $T_0$  in a 4-point probe configuration using<sup>[17,25]</sup>

$$R(T) - R(T_0) = m(T - T_0) = \beta R(T_0)(T - T_0) \quad (2)$$

The temperature coefficient of the resistance  $\beta$  and the slope of the resistance-temperature curve  $m = dR/dT$  were calibrated without an applied heating current, when the characterization platform was in a thermal equilibrium. For the characterization of  $\alpha$ , the thermovoltage  $V_{th}$  as well as the temperature difference  $T_{hot} - T_{cold}$  between  $RTD^{(1)}$  and  $RTD^{(2)}$  were measured.  $\alpha$  can then be evaluated as follows:

$$\alpha = \frac{-V_{th}}{T_{hot} - T_{cold}} \quad (3)$$

where  $V_{th}$  is the thermoelectric voltage between  $RTD^{(1)}$  and  $RTD^{(2)}$ ,  $T_{hot}$  is the temperature of  $RTD^{(1)}$  and  $T_{cold}$  is the temperature of  $RTD^{(2)}$ , respectively.

## 2.5. Thermal Conductivity Characterization Procedure

Figure 4c shows a schematic top view of the contact configuration for the measurement of  $\lambda$ . When a current is applied to the heating stripe, the heating power  $P$  is dissipated in the heating stripe causing a temperature gradient along the sample. Due to the symmetry of the transport device, we considered  $P/2$  for each side of the heating stripe. The thermal conductance  $G_{th}$  of one side of the device can then be evaluated using the following equation:

$$G_{th} = \frac{P/2}{\Delta T} \quad (4)$$

where  $\Delta T = T_1 - T_0$  is the temperature difference,  $T_1$  is the temperature at the heating stripe position  $x = 0$ , and  $T_0$  is the temperature of the Si substrate (heat sink) which corresponds to ambient temperature.  $P = I^2 R$  was determined from the

electrical resistance  $R$  of the heating stripe underneath the sample and the applied electrical current  $I$ .

In order to obtain  $\Delta T$  along the sample in  $x$ -direction (perpendicular to the heating stripe) we used three approaches, namely analytical, simulation, and experimental. The analytical approach is based on the 1D steady-state heat balance equation. By solving the 1D heat balance equation considering radiation loss and thermal conduction with the specific boundary conditions,  $\Delta T$  along the TE material in  $x$ -direction is given by

$$\Delta T(x) = (T_1 - T_0) \frac{\sinh(\sqrt{\mu}(L-x))}{\sinh(\sqrt{\mu}L)} \quad (5)$$

where  $\mu$  depends on the geometry, emissivity, and thermal conductivity of the TE material (see Section 4, Analytical Approach). In addition to the 1D analytical approach, we performed a 3D finite element method simulation using Comsol Multiphysics with the heat transfer and AC/DC modules and specific boundary conditions dedicated to the experimental

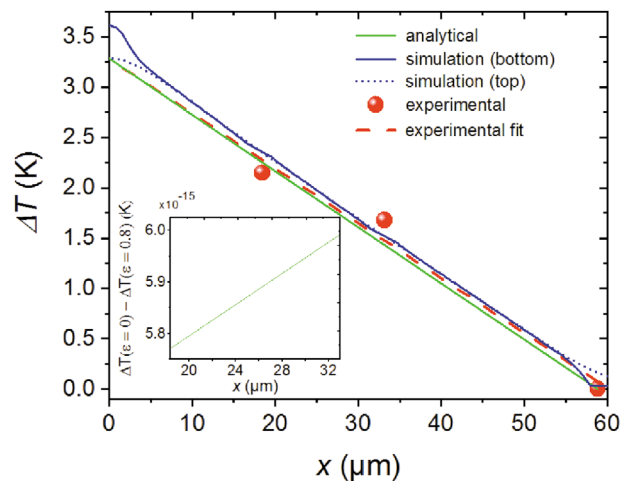


**Figure 5.** The temperature distribution depending on the position  $x$  starting at the position of heating stripe ( $x = 0$ ) up to the heat sink at the position ( $x = L$ ) for analytical (green), simulation (orange), and experimental (blue) model. The dashed red line shows the fitted line to experimental data. The inset shows deviation of the analytical results calculated for an emissivity of 0 and 0.8.

setup (see Section 4, Simulation). The temperature distribution depending on the position  $x$  (ranging from the center of the heating stripe at  $x = 0$  to the heat sink at  $x = L$ ) is shown in Figure 5. For the analytical result (green line) and the simulation (blue lines), an emissivity of 0.8 was used to study the influence of the radiation loss assuming a worst-case scenario (typical emissivity of  $\text{Co}_{75}\text{Ni}_{25}$  is  $<0.2$ ). Interestingly, the analytically calculated  $\Delta T$  as well as the simulation results show a linear behavior, that is, the influence of the radiation loss is negligible and the 1D approach is in good agreement with the 3D simulation. The inset of Figure 5 shows the deviation of the analytical results calculated for an emissivity of 0 and 0.8 confirming the negligible contribution of the radiation loss. Further, parasitic heat loss through the heating stripe and RTDs was investigated in terms of the thermal conductance of the TE material. For the  $\text{Co}_{0.75}\text{Ni}_{0.25}$  film, these parasitic effects can be neglected. In general, the product of  $\lambda d$  of the material should be larger than  $1.8 \times 10^{-4} \text{ W K}^{-1}$  to not exceed a measurement error of 10 % due to parasitic heat loss (see Supporting Information for details).

The simulated temperature distribution at the bottom of the sample shows a small deviation from the linear behavior at  $x = 0$ . This is caused by the heat flow in  $z$ -direction which was not considered in the 1D analytical approach. This only affects the direct environment of the heating stripe; a few micrometers away from the heating stripe, the temperature along the cross-section is homogenized, that is, does not depend on the  $z$ -direction (see Figure 5 simulation at bottom and top surface of the sample).

Since the temperature of the heating stripe is slightly higher than the average temperature of the cross-section at  $x = 0$ , we determined the temperature increase at  $x = 0$  by a linear regression. Therefore, we did a linear fit to the experimental data shown in Figure 5. There are three experimental data points corresponding to three  $x$  positions: the measured temperature of RTD<sup>(1)</sup> and RTD<sup>(2)</sup> as well as the ambient temperature  $T_0$ . The temperature of each RTD was calculated by evaluating its resistance increase as described in the previous section. The linear fit is consistent with experimental data as well as the hyperbolas of the analytical and simulation results. Therefore, the  $y$ -intercept extrapolated from this linear fit is a valid assumption for the mean temperature  $T_1$  of the sample cross-section at  $x = 0$ .

To calculate the thermal conductivity of the TE material, in addition to  $\Delta T$ , the heating power  $P$  has to be considered. Due to the small dimension of the heating stripe compared to that of the TE material, the heat losses of the heating stripe by both radiation and thermal conduction can be neglected. The radiation loss of the TE material is negligible as shown before. Therefore, the thermal conductivity can be obtained by (see Section 4, Analytical Approach)

$$\lambda = \frac{PL}{2A(T_1 - T_0)} \quad (6)$$

where  $A$  denotes the cross-section of the TE material.

## 2.6. Experimental Validation and Discussion

In this section, we summarize our experimental validation (see Section 4 for details of the experiments). Figure 6 shows the

temperature-dependent TE properties of the thick film measured with our transport device and an arc-molten bulk  $\text{Co}_{75}\text{Ni}_{25}$  reference sample, measured with commercial measurement technique, that is, thermal transport option (TTO) in a Dynacool physical properties measurement system and a laser flash analyser (LFA) from Linseis. Note that the error bars shown in the figures are results of the uncertainties calculated from the standard deviation of the measured properties and its error propagation in the used equations. The room temperature  $\sigma$  is  $8.27 \times 10^6 \text{ S m}^{-1}$  and  $8.56 \times 10^6 \text{ S m}^{-1}$  for thick film and bulk sample, respectively. The  $\sigma$  of the thick film measured with our transport device is in good agreement with that of the bulk sample except for the small deviations at lower temperatures (see Figure 6a).

Figure 6b shows the temperature-dependent  $\alpha$  for  $\text{Co}_{75}\text{Ni}_{25}$ . Both thick film and bulk sample possess a negative  $\alpha$  which indicates  $n$ -type conduction. The electrochemically deposited  $\text{Co}_{75}\text{Ni}_{25}$  thick film has a slightly lower relative  $\alpha$  than that of the arc-molten bulk sample.

The temperature-dependent  $\lambda$  of the  $\text{Co}_{75}\text{Ni}_{25}$  thick film is shown in Figure 6c. The  $\lambda$  of the arc-molten bulk sample shows a higher value than that of the thick film in the measured temperature range. There are a variety of factors such as grain size, porosity and impurities which affect transport properties of matter. Compared to the bulk sample, the electrochemically deposited  $\text{Co}_{75}\text{Ni}_{25}$  thick film has a stronger disorder within the grains and at the grain boundaries. Consequently, scattering at defects and grain boundaries becomes more dominant and reduces the mean free path of electrons and phonons. In general,  $\lambda$  consists of contributions of electrons  $\lambda_e$  and phonons  $\lambda_l$ . While in a pure metal  $\lambda$  is mostly dominated by  $\lambda_e$  contribution and  $\lambda_l$  is negligible in metallic alloys, electrons are strongly scattered by solute atoms which reduces the ability of electrons to carry heat and current.<sup>[26]</sup>

If the Wiedemann–Franz law holds, the electronic contribution is given by the relation  $\lambda_e = L_0 T \sigma$  where  $L_0$  is the Lorenz number. If we assume the experimental  $\lambda$  as  $\lambda_e$ , the calculated Lorenz number from the Wiedemann–Franz law at room temperature is  $2.14 \times 10^{-8} \text{ W } \Omega \text{ K}^{-2}$ , which is close to that of bulk Ni  $2.19 \times 10^{-8} \text{ W } \Omega \text{ K}^{-2}$  and Co  $1.98 \times 10^{-8} \text{ W } \Omega \text{ K}^{-2}$ .<sup>[26]</sup>

The electrochemically deposited  $\text{Co}_{75}\text{Ni}_{25}$  thick film has a  $PF$  of  $4.8 \text{ mW m}^{-1} \text{ K}^{-2}$  close to the measured bulk value of  $5.6 \text{ mW m}^{-1} \text{ K}^{-2}$ , but due to its relative high  $\lambda$  the  $zT$  value remains quit low. At room temperature the thick film has a  $zT$  value of 0.028 comparable to its measured bulk value of 0.024. The temperature-dependent  $PF$  and  $zT$  value of the thick film is shown in Figure 6d.

## 3. Conclusion

We developed a transport device based on a pre-structured microchip for full in-plane  $zT$  characterization of TE thick films prepared by electrochemical deposition. This transport device enables a simultaneous characterization of  $\sigma$ ,  $\alpha$  and  $\lambda$  of a suspended TE thick film eliminating the influence of the substrate and seed layer.

For the thermal conductivity measurement, we developed a 1D analytical model to evaluate the measurement data which we verified by 3D finite element simulations. Further, we

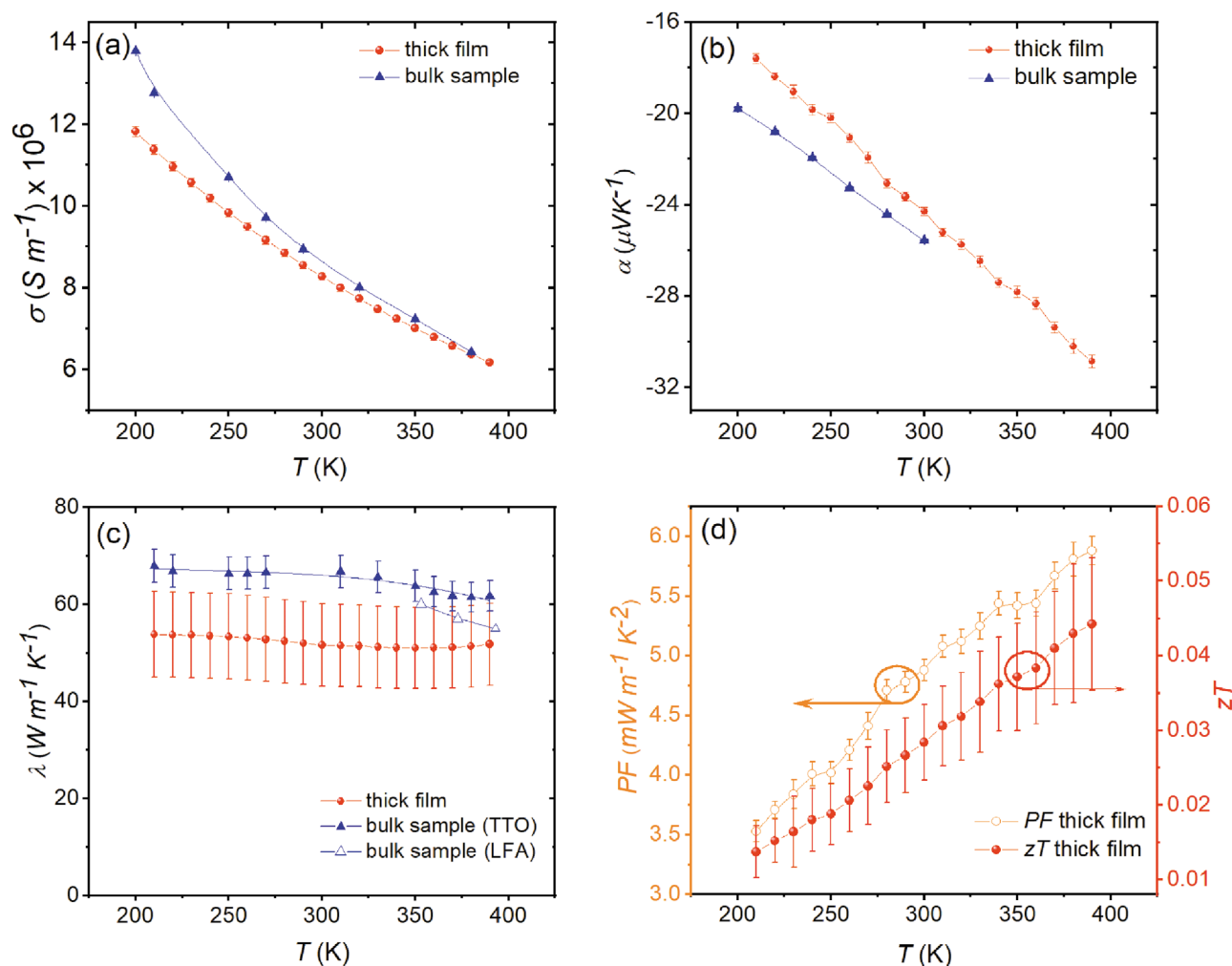


**Figure 6.** a) Measured  $\sigma$  of the  $\text{Co}_{75}\text{Ni}_{25}$  thick film using our characterization platform in comparison to the bulk sample, b) measured  $\alpha$  of the thick film in comparison to the bulk sample, c) measured  $\lambda$  of the thick film in comparison to the bulk sample measured with TTO in a Dynacool physical property measurement system as well as the LFA, and d) calculated  $zT$  and PF of thick film within the temperature range of 200–400 K.

determined the accuracy of the results taking into account the standard deviation of the measured properties and its error propagation in the used equations.

In addition, we characterized successfully temperature-dependent properties of  $\text{Co}_{75}\text{Ni}_{25}$  thick film within the transport device and compared them with those obtained for an arc-molten bulk sample. The thick film measurements were overall in a good agreement with the bulk measurement confirming the validity of our transport device. The observed deviations in the transport behavior of the two samples could be attributed to the differing microstructure.

In general, with our transport device it is possible to characterize samples in a wide temperature range from liquid He up to several hundred degrees Celsius. Our device also opens the possibility to perform magnetic field dependent measurements, which is especially interesting for magneto caloric and magneto Seebeck measurements that are usually not easily accessible. The device structure is scalable and therefore adaptable to other physical and chemical vapor deposition techniques.

## 4. Experimental Section

**Material Synthesis:** The thick film and bulk  $\text{Co}_{75}\text{Ni}_{25}$  samples were prepared by electrochemical deposition and arc melting, respectively.

**Electrochemical Deposition:** The  $\text{Co}_{75}\text{Ni}_{25}$  thick film was deposited directly on the pre-structured transport device using a Watts-type bath containing Co and Ni ions.<sup>[22]</sup> To enable a smooth and adherent electrochemical deposition, the transport device was cleaned for 2 min in an  $\text{O}_2$  plasma using RIE (Sentech SI220) with an  $\text{O}_2$  gas flow of 25 sccm at a power of 50 W before the deposition. The used Watts-type bath consisted of 0.18 mol  $\text{L}^{-1}$   $\text{CoSO}_4$  (99 %), 0.02 mol  $\text{L}^{-1}$   $\text{CoCl}_2$  (Fluka Chemika, 98 %), 0.95 mol  $\text{L}^{-1}$   $\text{NiSO}_4$  (98 %), 0.16 mol  $\text{L}^{-1}$   $\text{NiCl}_2$  (98 %), 0.73 mol  $\text{L}^{-1}$   $\text{H}_3\text{BO}_3$  (99.8 %), and 0.5 mol  $\text{L}^{-1}$   $\text{NaOH}$  to adjust the pH-value to 4–4.2 as described in Vega et al.<sup>[22]</sup> The electrochemical deposition was performed under pulsed potentiostatic conditions in a three-electrode configuration with a Pt counter electrode and Ag/AgCl reference electrode at room temperature using a BioLogic VSP modular five channels potentiostat. For the pulsed electrochemical deposition of  $\text{Co}_{75}\text{Ni}_{25}$ , a deposition potential of  $E_{\text{on}} = -1$  V was applied for  $t_{\text{on}} = 0.25$  s, followed by a relaxing time of  $t_{\text{off}} = 2$  s at an off potential of  $E_{\text{off}} = 0$  V. This parameters resulted in a  $\text{Co}_{75}\text{Ni}_{25}$  thick film with a thickness of 6  $\mu\text{m}$  after 24 min (640 pulses), which was measured with a profilometer (Bruker Dektak).

**Arc Melting:** As a reference sample, a Co<sub>75</sub>Ni<sub>25</sub> ingot was prepared by vacuum arc melting of Co (99.9 %) and Ni (99.7 %) granules. Before the melting under Ar atmosphere, the chamber was evacuated followed by purging with high purity Ar three times. During the melting process, the ingot was placed on a water-cooled Cu plate. The ingot was molten five times while flipping the sample after each melting step to ensure the same solidified condition of the ingot and make the microstructure uniformed. After arc-melting, the sample was sealed under vacuum (10<sup>-4</sup> mbar) in a fused silica tube and annealed at 1180 °C for 24 h. After annealing, the sample was quenched in a water bath.

**Analytical Approach:** The heat balance equation describes the heat flow given by heat conduction  $\dot{Q}_C$ , radiation  $\dot{Q}_R$ , and convection. In our case, convection can be neglected, since the characterization was carried out under vacuum (<10<sup>-5</sup> mbar). To calculate  $\Delta T$  in steady state, we considered the stationary heat balance equation  $\dot{Q}_R - \dot{Q}_C = 0$ . The radiation loss  $\dot{Q}_R$  of our sample is given by

$$\dot{Q}_R = \sigma_B(T(x)^4 - T_0^4)[(2b + 2d)\epsilon]dx \quad (7)$$

where  $\sigma_B$  is the Stefan–Boltzmann constant,  $\epsilon$  is the emissivity,  $d$  is the thickness, and  $b$  is the width of the TE material. For small temperature changes where  $(T(x) - T_0)T_0^{-1} \ll 1$ , we can use the approximation

$$T(x)^4 - T_0^4 \approx 4T_0^3\Delta T(x) \quad (8)$$

and by substituting Equation (8) in Equation (7) we obtain

$$\dot{Q}_R = 4\sigma_B T_0^3 \Delta T(x) [(2b + 2d)\epsilon] dx \quad (9)$$

The heat conduction by thermal conductivity  $\lambda$  in our sample is given by

$$\dot{Q}_C = -(\lambda d)b \frac{d^2\Delta T(x)}{dx^2} dx \quad (10)$$

The 1D steady state heat balance equation can then be written as

$$\frac{d^2\Delta T(x)}{dx^2} - \mu\Delta T(x) = 0 \quad (11)$$

with

$$\mu = \frac{4\sigma_B T_0^3 [(2b + 2d)\epsilon]}{(\lambda d)b} \quad (12)$$

$\Delta T$  in  $x$  direction can be obtained by taking into account the boundary conditions of our system. The origin of the  $x$ - $y$  coordinate system is set to the center of the membrane (see Figure 4c), the first boundary condition is defined on the heat sink,  $\Delta T(x=L) = 0$ . The second boundary condition is defined in middle of the heating stripe,  $\Delta T(x=0) = T_1 - T_0$ . By solving Equation (11) with the given boundary conditions,  $\Delta T$  along the TE material in  $x$  direction can be obtained as

$$\Delta T(x) = (T_1 - T_0) \frac{\sinh(\sqrt{\mu}(L-x))}{\sinh(\sqrt{\mu}L)} \quad (13)$$

To calculate  $\lambda$  of the TE material, in addition to  $\Delta T$ , the heating power  $P$  of one side of the symmetric device has to be obtained. Due to the small dimension of the heating stripe in comparison to the TE material, the heat losses of the heating stripe by both, heat conduction and radiation, can be neglected. Therefore, the heating power of the heating stripe  $P_0$  is given by

$$P_0 = -A\lambda \left. \frac{d\Delta T(x)}{dx} \right|_{x=0} \quad (14)$$

where  $A$  denotes the cross section ( $b \times d$ ) of our sample. Using  $\Delta T(x)$  from Equation (13) and taking into account that the heating power is equally distributed ( $P = P_0/2$ ), we obtain

$$P = 2A\lambda(T_1 - T_0)\sqrt{\mu} \cdot \coth(\sqrt{\mu}L) \quad (15)$$

If the radiation loss is negligible, Equation (15) can be developed in a Taylor series around  $\mu \rightarrow 0$  and the thermal conductivity is given by

$$\lambda = \frac{PL}{2A(T_1 - T_0)} \quad (16)$$

**Simulation:** To verify the 1D analytical approach used for the evaluation of the measurement data, a 3D Comsol Multiphysics simulation was used, which provides a finite element modeling and simulating of physics-based problems. For a thermoelectric analysis, heat transfer and electric current modules are applied, which can be coupled by thermoelectric effects to find solutions for Peltier, Seebeck, and Thomson effects. The governing equations that the model solves are as follows:

$$-\nabla((\sigma\alpha^2T + \lambda)\nabla T) - \nabla(\sigma\alpha T\nabla V) = \sigma((\nabla V)^2 + \alpha\nabla T\nabla V) \quad (17)$$

$$\nabla(\sigma\alpha\nabla T) + \nabla(\sigma\nabla V) = 0 \quad (18)$$

where  $T$  and  $V$  denotes the temperature and the voltage, respectively. The specific boundary conditions dedicated to experimental setup are as follows: The temperature of the heat sink fixed at  $T_0 = 300$  K was defined as the first boundary condition. An electrical current of  $I = 16$  mA was applied at the heating stripe, which generated  $T_1$  at the position of the heating stripe. Table S1, Supporting Information, shows the summarized parameters used in the Comsol simulation. Figure S1, Supporting Information, shows a 3D plot of the model geometry and an overview of the steady state temperature distribution along the sample at ambient temperature of  $T_0 = 300$  K. To increase the resistance of the heating stripe underneath the TE material, its cross-section was reduced in the relevant area. At the edges of the material, the cross-section of the heating stripe was increased building a trapezoid surface. This was done to create the maximum heating power underneath the TE material, since the  $P$  increases with decreasing cross-section. To only measure the electrical power converted to heat in the TE material, the voltage probes are placed close to the material.

**Thermoelectric Characterization:** The full  $zT$  characterization was performed in a Quantum Design Dynacool system in a temperature range from 200–400 K. For the arc-molten bulk characterization, the Quantum Design TTO in continuous mode was used. For the thick film characterization, the transport device was mounted to an electrical transport puck and connected to external devices. In order to measure the heating power and the current of the RTDs, two DC Sourcemeters (Keithley 2400) were used. The thermal voltages and the voltages for resistance measurement of the RTDs were measured by a Nanovoltmeter Keithley 2182A. The thermal conductivity of arc-molten bulk sample characterized with both TTO and LFA.

## Supporting Information

Supporting Information is available from the Wiley Online Library or from the author.

## Acknowledgements

The authors are grateful to Ronald Uhlemann, Tom Sieger, Heidrun Stein, and Cindy Kupka in Leibniz IFW Dresden for the technical support. V.B. gratefully thanks Ulrike Wolff for her support with scanning electron microscopy, Jens Freudenberger for providing the bulk sample, Amin Bahrami and David Alberto Lara Ramos for helpful discussions.

Financial support from the European Union (EU) and the Free State of Saxony through the European Regional Development Fund (ERDF) (SAB GroTEGx, grant no. 100245375) are acknowledged. J.G. acknowledges the financial support from the Principality of Asturias and European Union under the PCTI/FEDER program "Retorno Talento" (project no. IDI/2018/000010). L.U.S. acknowledges the funding of the Deutsche Forschungsgesellschaft (project no. NI 616/22-1). G.L. thanks the support by the startup funding from the Institute of Physics at the Chinese Academy of Sciences.

## Conflict of Interest

The authors declare no conflict of interest.

## Keywords

CoNi, electrochemical deposition, thermal conductivity, thermoelectrics

Received: November 21, 2019

Revised: January 5, 2020

Published online: February 3, 2020

- 
- [1] H. J. Goldsmid, *Introduction to Thermoelectricity*, Springer, Berlin **2010**.
- [2] G. J. Snyder, E. S. Toberer, *Nat. Mater.* **2008**, *7*, 105.
- [3] R. He, G. Schierning, K. Nielsch, *Adv. Mater. Technol.* **2017**, *3*, 1700256.
- [4] A. Shakouri, Y. Zhang, *IEEE Trans. Compon. Packag. Technol.* **2005**, *28*, 65.
- [5] R. Enright, S. Lei, K. Nolan, I. Mathews, A. Shen, G. Levaufre, R. Frizzell, G. H. Duan, D. Herson, *Bell Labs. Tech. J.* **2014**, *19*, 31.
- [6] J. Garcia, D. A. L. Ramos, M. Mohn, H. Schlörb, N. P. Rodriguez, L. Akinsinde, K. Nielsch, G. Schierning, H. Reith, *ECS J. Solid State Sci. Technol.* **2017**, *6*, N3022.
- [7] G. Li, J. G. Fernandez, D. A. L. Ramos, V. Barati, N. Pérez, I. Soldatov, H. Reith, G. Schierning, K. Nielsch, *Nat. Electron.* **2018**, *1*, 555.
- [8] N. Su, S. Guo, F. Li, D. Liu, B. Li, J. Li, M. Ji, *J. Micromech. Microeng.* **2018**, *28*, 125002.
- [9] J. P. Rojas, D. Singh, S. B. Inayat, G. A. T. Sevilla, H. M. Fahad, M. M. Hussain, *ECS J. Solid State Sci. Technol.* **2017**, *6*, N3036.
- [10] V. Leonov, R. J. M. Vullers, *J. Renewable Sustainable Energy* **2009**, *1*, 062701.
- [11] S. J. Kim, J. H. We, B. J. Cho, *Energy Environ. Sci.* **2014**, *7*, 1959.
- [12] J. Cancheevaram, R. Alley, E. Siivola, R. Venkatasubramanian, *MRS Online Proc. Libr.* **2004**, *793*, S8.18.1.
- [13] F. Völklein, H. Reith, A. Meier, *Phys. Status Solidi A* **2013**, *210*, 106.
- [14] Z. Bian, Y. Zhang, H. Schmidt, A. Shakouri, *24th Int. Conf. on Thermoelectrics*, IEEE, Piscataway, NJ **2005**, p. 76.
- [15] J. Xie, C. Lee, M. F. Wang, J. M. Tsai, *Microsyst. Technol.* **2011**, *17*, 77.
- [16] A. Sikora, H. Ftouni, J. Richard, C. Hébert, D. Eon, F. Omnès, O. Bourgeois, *Rev. Sci. Instrum.* **2012**, *83*, 054902.
- [17] M. F. Wagner, F. Völklein, H. Reith, C. Trautmann, M. E. Toimil-Molares, *Phys. Status Solidi A* **2016**, *213*, 610.
- [18] V. Linseis, F. Völklein, H. Reith, K. Nielsch, P. Woias, *Rev. Sci. Instrum.* **2018**, *89*, 015110.
- [19] R. Singh, Z. Bian, G. Zeng, J. Zide, J. Christofferson, H.-F. Chou, A. Gossard, J. Bowers, A. Shakouri, *Mater. Res. Soc. Symp. Proc.* **2005**, *0886*, F04.
- [20] M. M. Rojo, J. J. Romero, D. Ramos, D. A. Borca-Tasciuc, T. Borca-Tasciuc, M. M. Gonzalez, *Int. J. Therm. Sci.* **2015**, *89*, 193.
- [21] V. Linseis, Z. M. Hassan, H. Reith, J. Garcia, K. Nielsch, H. Baumgart, E. Redel, P. Woias, *Phys. Status Solidi A* **2018**, *215*, 1700930.
- [22] V. Vega, T. Böhnert, S. Martens, M. Waleczek, J. M. Montero-Moreno, D. Görlitz, V. M. Prida, K. Nielsch, *Nanotechnology* **2012**, *23*, 465709.
- [23] J. Garcia, V. Vega, L. Iglesias, V. M. Prida, B. Hernando, E. D. Barriga-Castro, R. Mendoza-Reséndez, C. Luna, D. Görlitz, K. Nielsch, *Phys. Status Solidi A* **2014**, *211*, 1041.
- [24] T. Böhnert, V. Vega, A. K. Michel, V. M. Prida, K. Nielsch, *Appl. Phys. Lett.* **2013**, *103*, 092407.
- [25] Y. Tian, M. R. Sakr, J. M. Kinder, D. Liang, M. J. MacDonald, R. L. Qiu, H. J. Gao, X. P. Gao, *Nano Lett.* **2012**, *12*, 6492.
- [26] T. M. Tritt, *Thermal Conductivity Theory, Properties, and Applications*, Springer, New York **2004**.